Schweizerische Eidgenossenschaft
Confédération suisse
Confederazione Svizzera
Confederaziun svizra

Eidgenössisches Departement für
Umwelt, Verkehr, Energie und Kommunikation UVEK

Bundesamt für Energie BFE

GEO-TEP

DEVELOPMENT OF THERMOELECTRIC MATERIALS FOR GEOTHERMAL ENERGY CONVERSION SYSTEMS

Schlussbericht 2008

Ausgearbeitet durch

Laura Bocher and Anke Weidenkaff
Solid State Chemistry and Catalysis, Empa-Swiss Federal Laboratories for Materials Testing and Research
Ueberlandstrasse 129, CH-8600, Dübendorf

laura.bocher@empa.ch, anke.weidenkaff@empa.ch, www.empa.ch

Impressum

Datum: *04. Dezember 2008*

Im Auftrag des Bundesamt für Energie
Forschungsprogramm Elektrizitätstechnologien und -anwendungen

Mühlestrasse 4, CH-3063 Ittigen

Postadresse: CH-3003 Bern

Tel. +41 31 322 56 11, Fax +41 31 323 25 00

www.bfe.admin.ch

BFE-Bereichsleiter, michael.moser@bfe.admin.ch

BFE-Vertrags- und Projektnummer: 151615

Bezugsort der Publikation: www.energieforschung.ch / www.electricity-research.ch

Inhaltsverzeichnis

Zusammenfassung

Mit geeigneten thermoelektrischen Konvertern kann Wärmeenergie aus geothermischen Quellen direkt in Elektrizität gewandelt. Da die Wandlung auf einer intrinsischen Materialeigenschaft der thermoelektrischen Materialien beruht, sind diese zunächst zu optimieren. In der vorliegenden Arbeit wurden umweltfreundliche robuste oxidische Keramiken für eine solche potentielle Anwendung entwickelt.

Manganate sind hervorragende Kandidaten für potentielle direkte Energiewandler. Für die Untersuchung wurden verschiedene perowskitartige Materialien mittels innovative Synthesemethoden hergestellt. Das Synthese-Spektrum reichte von keramischen Methoden über innovative chimie-douce Methoden zu Aerosolprozessen. Zudem wurden die Materialien eingehend mittels Röntgen- und Elektronendiffraktionstechniken charakterisiert und für die Anwendung hinsichtlich der thermochemischen Stabilität themogravimetrisch getestet.

Die thermoelektrische Gütezahl ZT der Materialien konnte durch das gewonnene verbesserte Verständnis der Struktur-Eigenschaften-Beziehungen von dem ursprünglichen ZT von 0.021 auf 0.3 über eine weiten Temperaturbereich erhöht werden, welches die Materialien zu den bisher besten *n*-leitenden perowskitartigen Materialien macht. Zudem haben die Arbeiten gezeigt, dass eine weitere Steigerung der thermoelektrischen Aktivität durch Änderungen der Zusammensetzung und Mikrostruktur möglich sind. Es sind aber dazu noch erhebliche Forschungsanstrengungen erforderlich.

Abstract

Geothermal heat can be directly converted into electricity by using thermoelectric converters. The Thermoelectric conversion relies on intrinsic materials properties which have to be optimised. In this work novel environmentally friendly and stable oxide ceramics were developed to fulfil this task. Thus, manganate phases were studied regarding their potential thermoelectric properties for converting geothermal heat into electricity. Perovskite-type phases were synthesized by applying different methods: the ceramic route, and innovative synthesis routes such as the “chimie douce” method by bulk thermal decomposition of the citrate precursor or using an USC process, and also the polyol-mediated synthesis route. The crystal structures of the manganate phases are evaluated by XRPD, NPD, and ED techniques while specific microstructures such as twinned domains are highlighted by HRTEM imaging. Besides, the thermal stability of the Mn-oxide phases in air atmosphere are controlled over a wide temperature range ($T < 1300$ K).

The thermoelectric figure of merit ZT was enhanced from 0.021 to 0.3 in a broad temperature range for the studied phases which makes these phases the best perovskitic candidates as *n*-type polycrystalline thermoelectric materials operating in air at high temperatures.

1. Introduction

Global energy demand is becoming an increasingly problematic issue for the society and requires an immediate response from science. The development of renewable energy technologies is demanded for counteracting the strong dependence on limited fossil resources. The heat emitted from boundless sources such as geothermal heat can be efficiently converted for generating electricity by means of thermoelectric (TE) technologies. A TE module is composed of *p*- and *n*-type thermoelements which are connected electrically in series and thermally in parallel, as presented in Figure 1.

The efficient conversion of heat into electricity requires the development of functional materials with a high figure of merit, $Z = S^2/\rho\kappa$, where S is the Seebeck coefficient, ρ is the electrical conductivity and κ is the thermal conductivity.

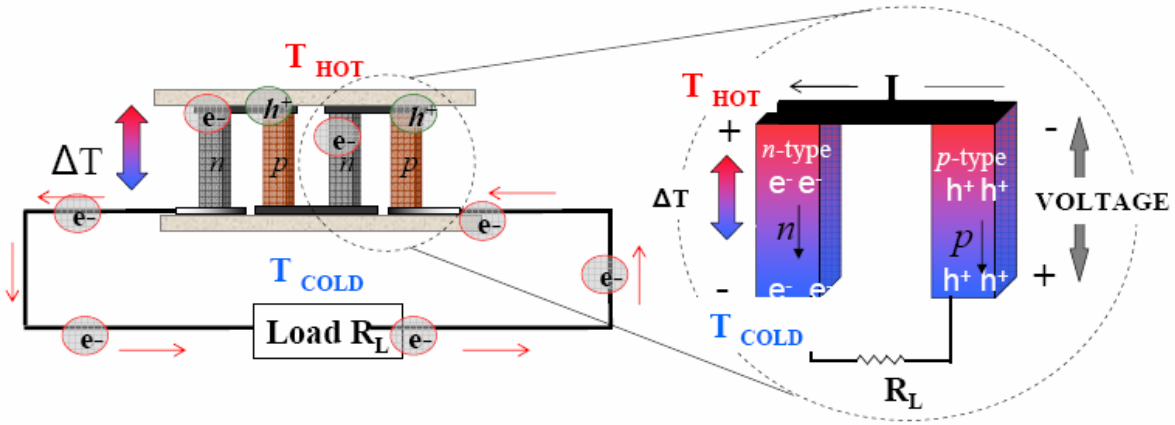

Figure 1: The conventional *p*/*n* configuration of a TE module. Right scheme highlights the electricity generation principle based on *p*- and *n*-thermoelements.

2. Scope of the work

To date, most commercial thermoelectric devices make use of $(Bi,Sb)_2(Te,Se)_3$-based alloys materials, which present high ZT values (ZT ~ 1). However, these conventional thermoelectric materials present important drawbacks, since they are composed of scarce and toxic elements, and present chemical instability at high temperatures in oxidative atmospheres. In respect to the environmental sustainability, the TE materials should belong to chemical systems without toxic elements such as tellurium, antimony and lead. Cost-efficient materials would be expected. Long-term utilizations can be achieved with thermoelectric modules since they have the advantage to be maintenance-free. Therefore, the reliability and the durability are essential prerequisites for TE technologies. The chemical, thermal and mechanical stabilities are required with respect to specific operating conditions (temperatures and atmospheres). Oxide thermoelectric materials are cost efficient and nontoxic compared to the

conventional phases. They are also chemically and thermally stable at high temperatures in oxidative atmospheres.

Targeting the best *p*- and *n*-TE materials imply to seek for materials with high ZT values and similar thermoelectric properties for both thermoelements at a specified operating temperature, i.e. large *S*, low ρ and κ. In this respect, complex metal oxides have proven to be promising TE candidates, especially layered cobaltate structures as well as perovskite-type phases, with the general formula ABO_3. Perovskite-type phases have very attractive physical-chemical properties coupled with a flexible crystal structure [Galasso-1969]. Thus, properties of perovskites can be modified and fine-tuned in a controlled way by cationic substitutions and changes in oxygen content. The challenge is to concurrently reduce the thermal conductivity, κ, defined as the sum of an electronic and a lattice component (κ_e and κ_l, respectively). In oxide materials κ_l prevails since phonons are the predominant heat carriers. Therefore, different strategies to lower the lattice heat conduction by phonon scattering are pursued. Phonon scattering may be promoted by complex crystal structures (e.g., perovskite structures) with several atoms per unit cell, by nanometer-sized crystallites due to an increasing amount of grain boundaries [Hicks-1993] and by the introduction of foreign atoms acting as additional scattering centers.

Terasaki et al. first reported in 1997 on an unusual large thermopower in metallic Na_xCoO_2 single crystal [Terasaki-1997]. Over the past decade, an active research interest, mainly in Japan and in Europe, explored the wide family of oxides allowing the identification of several thermoelectric oxide materials. Perovskite-type phases such as, for example, manganate [Bocher-2008a], titanate [Ohta-2006], or cobaltate [Robert-2007a] phases reveal large Seebeck coefficients, one of the essential prerequisites for potential TE materials. The large thermopower values are caused by a strong interplay between charge, electron spin states, and crystal structure [Maignan-1998, Hejtmanek-1999].

The unsubstituted manganate phases such as $LaMnO_3$ and $CaMnO_3$ are both antiferromagnetic insulators and exhibit large absolute Seebeck coefficients, i.e. S = 450 $\mu V\ K^{-1}$ for $LaMnO_3$ and S = -350 $\mu V\ K^{-1}$ for $CaMnO_3$ at 300 K [Autret-2005; Maignan-1998]. Manganate phases having *p*- or *n*-type conduction are successfully accomplished by aliovalent substitutions either on the A- or the B-site in both $RMnO_3$ and $AMnO_3$ insulating systems. In particular, electron-doped manganates show promising thermoelectric properties at elevated temperatures (*T*.>> 300 K) [Flahaut-2006, Thao-2003]. While comprehensive studies are available on the improvement of transport properties of manganate phases, the thermal conduction behavior of complex metal oxides has not been intensively investigated so far. A reduction of the thermal conductivity, $\kappa(T)$, might be achieved without affecting the power factor by adjusting the particle morphology and microstructure. The present work is dedicated on the development of functional manganate thermoelectric materials having enhanced Figure of Merit.

3. Method

Polycrystalline $CaMn_{1-x}Nb_xO3$ (with $x < 0.30$) and $LaMn_{1-x}Co_xO3$ (with $x = 0.05, 0.10, 0.90,$ and 0.95) perovskite-type phases were prepared by different synthesis methods: by a conventional solid state reaction (SSR) method, by a "*chimie douce*" synthesis, and by a polyol-mediated (PM) synthesis method. The polymeric precursor synthesised by the "*chimie douce*" route was thermally decomposed either by stepwise calcinations (SC) or by an ultrasonic spray combustion (USC) process [Bocher-2007]. The implemented SC method consisted of the preparation of complex precursors, which were subsequently decomposed by stepwise calcination with particular attention to low synthesis temperatures ($873 K < T < 1073 K$) [Weidenkaff-2004].

Different techniques allow the characterization and the evaluation of the TE materials. The crystallographic parameters were determined by X-ray powder diffraction (XRPD), neutron powder diffraction (NPD) and electron diffraction (ED). Non-ambient in situ diffraction experiments were performed in terms of high-temperature XRPD and ED techniques and low-temperature NPD method. The morphological and microstructural features of the synthesised oxides were studied by scanning- and transmission electron microscopy (SEM and TEM, respectively). The cationic compositions were evaluated by energy dispersive X-ray and X-ray photoemission spectroscopies (EDS and XPS, respectively). In addition, electron energy loss spectroscopy (EELS) was performed in a dedicated scanning transmission electron microscope (STEM) to combine imaging and spectroscopic capabilities at the nanoscale. Thermogravimetric analyses (TGA) were performed for studying the thermal decomposition/stability and the anionic composition of the perovskite-type manganate phases. The transport and thermal properties, i.e. the Seebeck coefficient *S*, the electrical conductivity ρ and the thermal conductivity κ were measured over a wide range of temperature ($5 K < T < 1240 K$). The high-temperature thermal conductivity ($T > 300 K$) was indirectly determined via the thermal diffusivity α and the specific heat capacity *Cp*, respectively measured by laser flash apparatus (LFA) and differential scanning calorimetry (DSC). The magnetic properties were measured at low temperatures ($T < 350 K$) by both physical property measurement system (PPMS) and superconducting quantum interferences device (SQUID).

3.1 Crystal structure, microstructure and composition determination:

The phase purity and the crystal structure of the manganate phases were determined by XRPD and NPD technique at room temperature. Besides, magnetic transition was investigated at low temperatures by NPD technique and the high-temperatures structural transition was studied by XRPD method. Crystallographic parameters were obtained from Rietveld refinements of the XRPD and/or NPD data using the Fullprof program [RodriguezCarvajal-1993].

The electron microscope is a versatile instrument to investigate the microstructure of materials, to identify new or known phases by electron diffraction (ED), and to yield information on compositions using energy X-ray dispersive spectroscopy (EDS). XRPD technique provides averaged crystallographic information of the studied phases. ED is an essential tool allowing the analysis of local structures within the crystal, beyond the capability of X-ray or neutron techniques. Thus, XRPD, NPD, and ED techniques were used as complementary methods.
High resolution transmission electron microscopy (HRTEM) images reveal local structures of crystals in great detail. The local crystallinity and microstructure of the manganate phases were studied by ED and HRTEM, respectively. Furthermore, experimental investigations on the $CaMn_{0.92}Nb_{0.08}O_3$ phase were performed on SuperSTEM2, an aberration-corrected instrument, at the UK's SuperSTEM national facility. It provides atomic column chemical and electronic information of the materials properties by combining HAADF and EELS, respectively [Bleloch-2004]. High resolution DF images could emphasize Z-contrast on detailed microstructure, e.g. twinned domain boundaries. EELS spectra of Ca, Mn, Nb and O were recorded providing several information such as the electronic states of manganese atoms. Besides, local changes in the oxidation manganese states could be determined at domain boundaries by ELNES analysis.

3.2 Thermoelectric properties measurements at high temperature (T > 300 K):

The thermoelectric properties of a material are evaluated from the measurement of the Seebeck coefficient *S*, the electrical resistivity ρ, and the thermal conductivity κ.
The thermal conductivity of bulk materials can be determined by the laser-flash thermal diffusivity method: the thermal conductivity κ is related to the thermal diffusivity α, the specific heat capacity Cp, and the relative bulk density d by the following equation: $\kappa = d * \alpha * Cp$. The relative bulk density was measured by the Archimedes method. The principle of the flash method is illustrated in Figure 2a). This instrument uses a solid-state laser (λ) 1064 nm) to heat one side of the polycrystalline sample and an InSb infrared detector to measure the corresponding heat increase on the back side. The thermal diffusivity of the manganate phases was measured using a Netzsch LFA (Laser Flash Apparatus) 457 Microash system (Figures 2 b) and c). The thermal diffusivity of a disc-shaped sample (~ 1 mm thickness * 10 mm diameter) was determined in different atmospheres (air or argon, with a gas flow rate of 50 mL min^{-1}) between 300 K and 1273 K at a heating rate of 5 K min^{-1}. Measurements were performed every 50 K and repeated 5 times at each temperature. The thermal diffusivity measurements were evaluated thanks to the Netzsch Proteus LFA analysis software, including modelling correction methods.

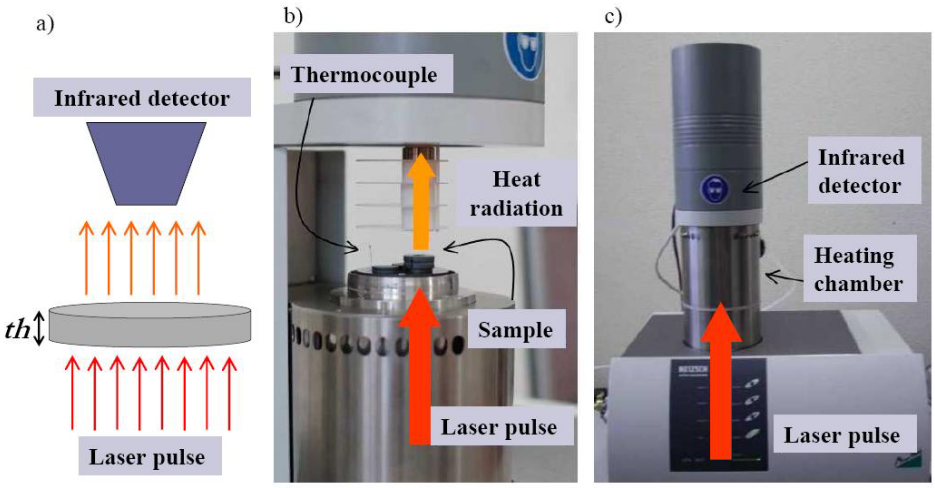

Figure 2 :Schematic representation of the flash method principle, b) and c) magnification and large view of the Netzsch LFA 457 Microflash thermal diffusivity instrument, respectively.

The electrical resistivity and the Seebeck coefficient of the manganate phases were determined over a wide temperature range, under different atmospheres, and upon heating/cooling cycles. The measurements were performed on bar-shaped samples (~ 1.5 * 1 * 5 mm^3) using a RZ2001i unit from Ozawa Science (Japan). Electrical resistivity and thermopower values were measured every 20 K in a temperature range of 320 K < T < 1240 K while heating and then cooling.

3.3 Magnetic, electrical and thermal transport properties measurements at low temperature (T < 400 K):

The low-temperature measurements (S, ρ and κ) were performed using the commercial thermal transport option (TTO) puck from Quantum Design. The measurements were performed on bar-shaped samples (~ 1.5 * 1 * 5 mm^3) in a temperature range of 5 K < T < 350 K, using a physical properties measurement system (PPMS) from Quantum Design. The magnetic susceptibility of the manganate phases was measured with a vibrating sample magnetometer (VSM) in PPMS device or with a superconducting quantum interference device (SQUID) magnetometer. Magnetic susceptibilities were measured during zero-field cooled (zfc) measurement upon heating, then a magnetic field was applied in the paramagnetic temperature region (e.g. at T ~ 300 K) to perform a field cooled (fc) measurement upon heating.

4. Results and Discussions

4. 1. Synthesis

The classical solid state reaction (SSR) method, as known as conventional ceramic route, results typical sintered micrometer-size grains, leading to a compact and dense structure. While good thermoelectric properties are achieved for phases having low-level cationic substitutions, the homogeneous distribution of substituted elements is rather difficult to obtain

applying this preparation method. Therefore, alternative synthesis methods were developed for fine-tuning the particle shape and size of potential thermoelectric perovskite phases. A general overview on the different applied synthesis methods with an emphasis on the particle morphologies is given in Figures 3. All these synthesis methods proved to be successful methods for synthesizing cobaltate-[Robert-2007a], titanate- [Bocher-2007] or manganate [Bocher-2008a] phases at relatively low temperatures (T < 1000 K). In the present work, thermoelectric perovskite-type phases are synthesised by different methods to investigate the influence of the morphology and the microstructure on their thermoelectric properties.

Stepwise calcinations (SC): In SC processes, the cations of the perovskite phase are mixed in liquid solution, while in conventional ceramic methods, the interdiffusion of the cations in a solid matrix is necessary to homogenize the product phases. Thus, low substitution level can be fast and homogeneously distributed in the cationic network by using citric acid as a chelating agent for all cations in the aqueous solution. Another advantage of the SC synthesis route originates from the decomposition of the polymeric precursors, leading to submicrometer-size sintered grains interconnected in a particular way, as shown in Figure 3 a).

Ultrasonic Spray Combustion (USC): The USC method allows decomposing microdroplets of the citrate precursor solution flowing in a high temperature furnace by a continuous process. The USC process yields nanocrystalline perovskite particles forming hollow microspheres as presented in Figure 3 b). ultrafine USC particles present a relatively large specific surface area (50-60 m^2 g^{-1}) [Bocher-2007]. Citrate precursor concentration, gas flow rate, furnace temperature have to be adjusted to optimize the production rate while obtaining uniform ultrafine perovskite particles.

Polyol-mediated synthesis (PM): The PM synthesis route relies on the use of polyalcohols with high boiling temperature and sufficient ability to solve inorganic salts at elevated temperature. On the other hand, the polyol acts with a chelating effect avoiding agglomeration of particles during preparation. Crystalline manganate particles are obtained by the PM method and form a sponge-like highly-porous network, as shown in Figure 3 c), which could be as template for potential thermoelectric perovskite composite.

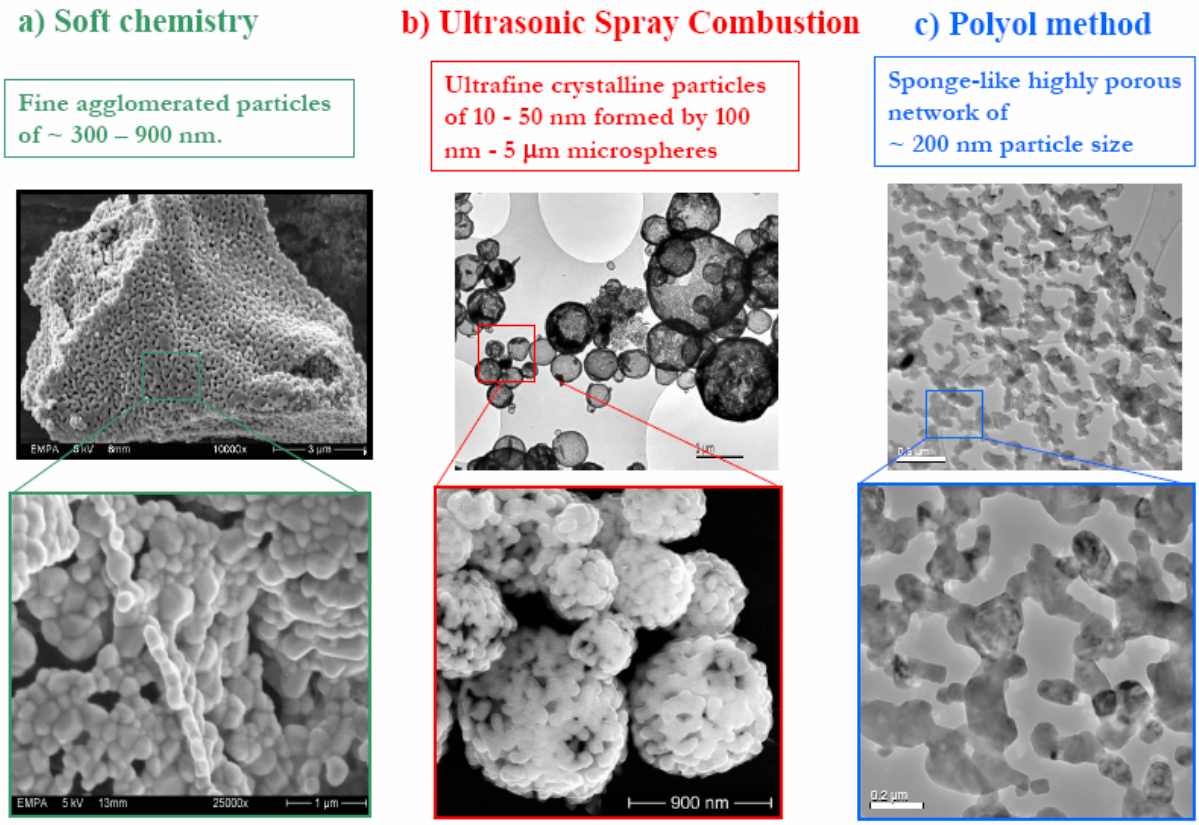

Figure 3: Different particle morphologies obtained from the various applied synthesis methods.

4. 2. $LaMn_{1-x}Co_xO3$ perovskite-type phases [Bocher-2006]

Submicrocrystalline particles of $LaMn_{1-x}Co_xO_{3\pm\delta}$ (with x = 0.05, 0.10, 0.90 and 0.95) have been synthesized by a *chimie douce* synthesis process to evaluate their thermoelectric properties. The morphology of the dense sintered pellets shows two different microstructures depending on the predominant transition metal (Figures 4, on top). Both pellets present a comparable relative density (≈ 90%). The morphology of the Co-rich pellet appears as compacted polyhedral grains with an inhomogeneous size distribution. The structure of the Mn-rich pellet present individual sintered particles mixed with sheet-like agglomerated particles. The Mn-rich pellets appear less agglomerated with smaller crystallites.

The Co-rich compounds crystallize in rhombohedral structure (*R-3c*) while the Mn-rich compounds present microdomains of orthorhomic structure (*Pbnm*). Figure 4 b) represents the intergrowth of microdomains with zone axis $[010]_p$ and $[100]_p \leftrightarrow [1\text{-}10]_o$ in which the long c-axis (d ≈7.8 Å) alternates at random in different regions of the crystal, along the three space directions. The domains present a long range of ordering without any defect or dislocation.

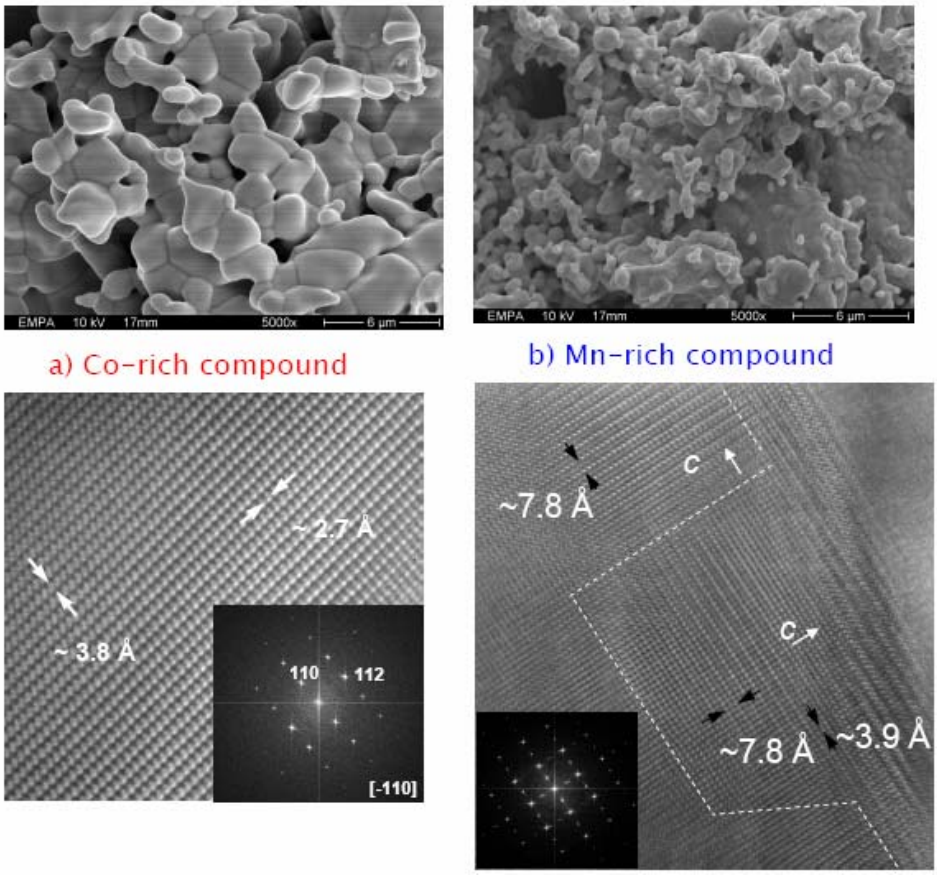

Figures 4: SEM pictures (on top) and HRTEM images (on bottom) of a) $LaMn_{0.10}Co_{0.90}O_{3+\delta}$ and b) $LaMn_{0.90}Co_{0.10}O_{3+\delta}$.. The high-resolution TEM image of the Mn-rich phase shows twinned domains. The FFT is indexed in cubic perovskite $a_p \times a_p \times 2a_p$. The long c axis of the supercell ($c = 2a_p = 7.8$ Å) is randomly distributed. HREM images of $LaMn_{0.10}Co_{0.90}O_{3-\delta}$ indexed as rhombohedral structure (*R3c*: a = 5.44Å, c = 13.11 Å).

The predominance of the transition metal influences strongly the transport and thermal properties of the perovskite-type phases. Low level of substitution increases the carrier concentration leading to a reduction of the absolute Seebeck value. The substitution of Mn by Co in the $LaMnO_3$ matrix induces a Mn^{3+}/Mn^{4+} mixed valency behaving as a *p*-type doping. The Mn-rich compounds (x = 0.05 and 0.10) exhibit positive Seebeck coefficient up to 700K, indicating predominant hole-like carriers. *n*-type doping is generated by the Co^{2+}/Co^{3+} mixed valency due to the substitution of Co by Mn in the $LaCoO_3$ system. With 5 % of Mn in the $LaCoO_3$ system, a negative Seebeck value is obtained at 340 K which indicates predominant electron-like carriers ($S_{340K} = -82.1 \mu V K^{-1}$).

The thermal properties are found to exhibit different features due to the distinct charge transport behavior depending on the predominant transition metal in the $LaMn_{1-x}Co_xO_{3\pm\delta}$ system (Figure 10). For the Mn-rich compounds (x = 0.05 and 0.10) the thermal conductivity is increased slightly with increasing the temperature. The manganate-rich compounds present a typical low thermal conductivity $\kappa_{340\,K} < 1.5\ Wm^{-1}K^{-1}$ for substituted $LaMnO_3$ The heat conduction for these compositions is mainly due to the phonons contributions. On the other hand the

Co-rich compounds reveal from 500 K an important increase of the electronic component concerning the thermal conductivity. This electronic predominance at high temperatures is due to the metallic conduction tendency of the Co-rich compounds. Below 500 K the cobaltate-rich compounds display low thermal conductivity values ($\kappa < 2$ $Wm^{-1}K^{-1}$). In the temperature range of 600 K < T 800 K, the Co-rich compounds show interesting features concerning theirs thermoelectric properties. A ZT value of 0.021 is reached for the $LaMn_{0.10}Co_{0.90}O_{3+\delta}$ compound at 700 K.

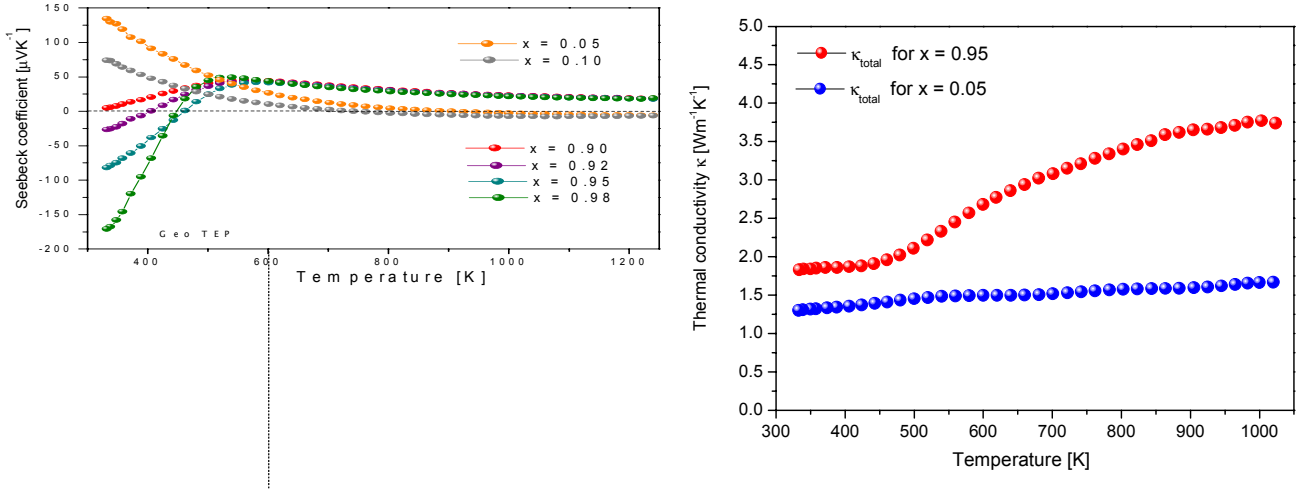

Figure 5: Temperature dependence of a) the Seebeck coefficient and b) the thermal conductivity for the $LaMn_{1-x}Co_xO_{3\pm\delta}$.

4. 3. $CaMn_{1-x}Nb_xO3$ perovskite-type phases

The present work reports on the highest ZT value obtained among electron-doped manganates phases (ZT > 0.3 at 1073 K), considering as the best perovskitic *n*-type polycrystalline thermoelectric materials operating in air at high temperatures [Bocher-2008b].

Perovskite-type $CaMn_{1-x}Nb_xO_{3-\delta}$ (x = 0.02, 0.05, 0.08, and 0.10) compounds were synthesized by applying the “chimie douce” (SC) synthesis, the USC process and the classical solid state reaction (SSR) method. $CaMn_{1-x}Nb_xO_{3-\delta}$ (x < 0.10) phases crystallize in the orthorhombic type structure, *Pnma* space group with the cell parameters ~ $a_p\sqrt{2} \times 2a_p \times a_p\sqrt{2}$, corresponding to the $a^+b^-b^-$ type tilting (a_p ~ 3.74 Å refers to the lattice parameter for the ideal cubic perovskite structure). The B-site Nb substitution causes an increasing of the lattice parameters and cell volume. Grains of 3-10 μm size are achieved for SSR phases, while the grain size of SC-derived phases is on the nanoscale (500-900 nm in diameter). The SEM study of the SSR compounds suggests a compact sintering between the grains due to a longer sintering process at higher temperatures. In contrast, the submicrometer-sized SC grains are particularly interconnected with channels running randomly between the sintered particles. Figures 6) illustrate the presence of nano-twinned domains, observed in the $CaMn_{0.98}Nb_{0.02}O_3$ phase. This finding indicates that moving from A1 to B1 across the domain

boundary is similar as rotating the orthorhombic unit cell by 90_ respect to [010]o, de_ned [010]90° . This specific microstructure is commonly described as rotation twins across f101go [Wang-2006]. The orthorhombic lattice parameters deviate slightly from the equivalent cubic ones, i.e. $a_p\sqrt{2}$ * 2ac * $a_p\sqrt{2}$ in the orthorhombic framework [Mitchell-2002]. Therefore, domains with specific orientations of the unit cell can growth coherently on each other yielding a twinning phenomenon.

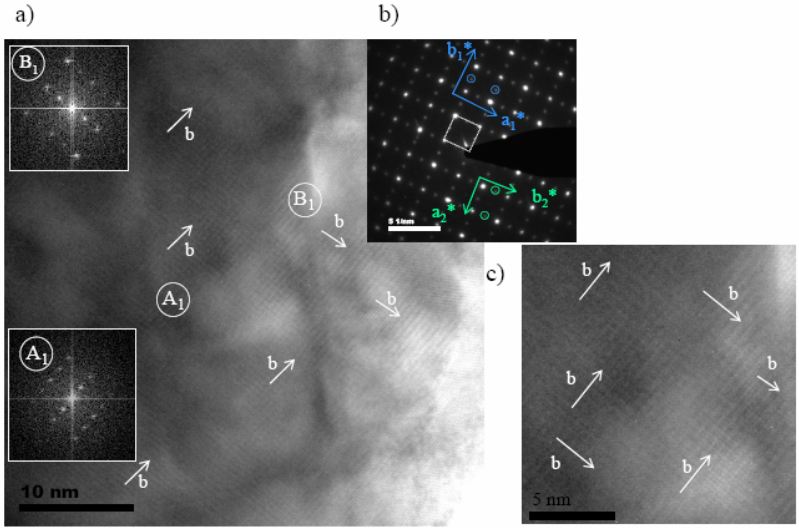

Figure 6: a) HRTEM, b) ED pattern of CaMn0.98Nb0.02O3 phase and c) magnified region of the nano-scale twinned domains where the b axis is oriented along two different directions in the plane. The inset in Figure a) present the fast Fourier transform (FFT) of the domains A1 and B1.

As previously reported, at low temperatures (T < 200 K), the resistivity for the $CaMn_{1-x}Nb_xO_3$ series (x < 0.08) increases with decreasing temperature, indicating semiconducting properties ($d\rho/dT < 0$) [Raveau-2000]. The electrical transport properties change gradually with the temperature. At higher temperatures (200 K < T < 1070 K), the electrical resistivity of both the SSR and the SC compounds drops to values as low as those characteristic for metals, for example, for the SC phases: for x = 0.05, ρ_{400K} = 12.1 mΩ cm. The introduction of a pentavalent cation such as Nb^{5+} generates Mn^{3+} ($e_g^1t_{2g}^3$) cations in the Mn^{4+} ($e_g^0t_{2g}^3$) matrix. Electrons in the e_g orbitals act as charge carriers in the Mn^{4+}-O-Mn^{3+} ion framework. The band structure and the carrier concentration vary with the extent of Nb substitution. The transport of charge carriers in manganate phases is generally well described by the small polaron hopping model; that is, the formation of polarons is defined as the combination of carriers with its strain field [Maignan-1998, Hejtmanek-1999]. Thus, the resistivity decreases with increasing charge carrier concentration.

All compounds present large negative thermopower values, that is, $|S| > 100\ \mu V\ K^{-1}$, in the temperature range from 300 to 1070 K (Figure 7), indicating that electrons are the predominant charge carriers. Identical thermopower values and $S(T)$ behavior are measured for the compounds with equivalent Nb content irrespective of the synthesis method. This confirms that the different microstructures of the SSR and SC phases do not influence either the charge carrier concentration or the electronic band structure. Increasing the Nb content in the

Mn sublattice leads to a decrease in absolute Seebeck coefficients from S_{900K}=-248 μV K^{-1} for x = 0.02 to S_{900K} = -150 μV K^{-1} for x = 0.08 following the Heikes law at high temperatures. This is explained by an increase in the charge carrier concentration inducing a decrease in the electrical resistivity. The largest Seebeck coefficients are obtained for both SSR and SC compounds with 2% Nb substitution (S_{1000K}) -251 μV K^{-1}). As a general tendency, the Seebeck coefficient exhibits a linear temperature dependence in the paramagnetic region; that is, |S| values increase with increasing temperature.

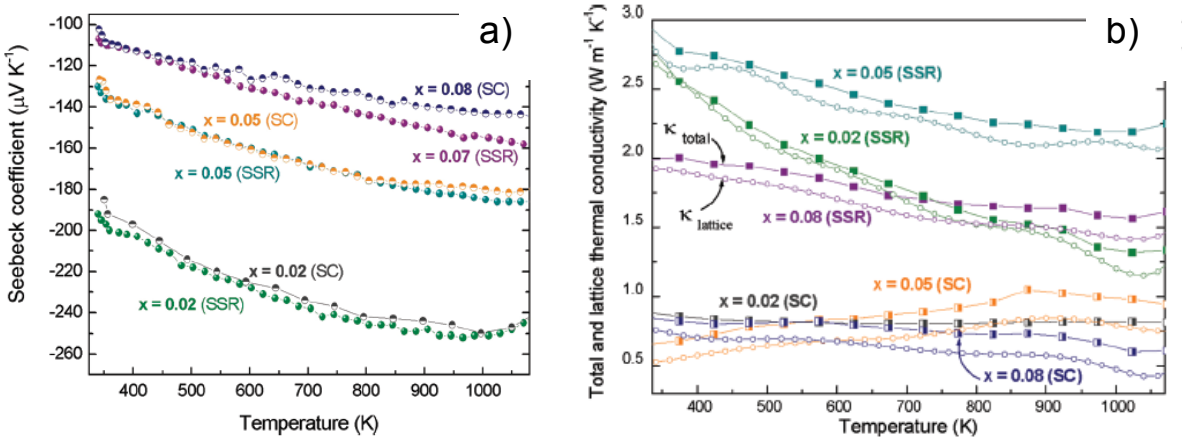

Figure 7: Temperature dependence of a) Seebeck coefficients and b) thermal conductivity for $CaMn_{1-x}Nb_xO_{3-\delta}$ (x = 0.02, 0.05, 0.08) synthesized by both a SSR (closed symbols) and a SC (half-open symbols) method.

Figure 7b) displays the total thermal conductivity and the lattice contribution (340 K < T < 1070 K) for all of the studied compounds. The electronic component, κe, can be estimated from the electrical resistivity data using the Wiedemann-Franz law (κe) $L_oT\sigma$, where L_o) 2.45 × 10^{-8} W Ω K^{-2} is the Lorenz number and σ is the electrical conductivity). Since κ_e does not exceed 20% of the total thermal conductivity, heat conduction is predominantly represented by the lattice component, κ_l. As for the SSR compounds, the total heat conductivity, κtotal, shows a common temperature dependence, that is, κ_{total} decreases slightly with increasing temperature. This behavior does not apply for the SC phases and might be related to generally lower thermal conductivities of SC compounds (κtotal < 1 W m^{-1} K^{-1}) compared to the SSR phases (1.5 W m^{-1} K^{-1} < κ_{total} < 3.0 W m^{-1} K^{-1}), which show typical values for oxide materials. The occurrence of twinned domains, shown by the HRTEM image in the SC phases, can be explained crystallographically. In comparison, twinned domains could be also identified in the SSR series by ED patterns. However, the size of the SC crystallites is smaller (200 nm diameter) than that of the SSR crystallites (in the micrometer range), leading to twinned domains of different dimensions. Lower thermal conductivity values, implying higher phonon scattering in SC phases, might result from the nanosized twinned domains or the porous morphology.

Figure 8 presents the dimensionless figure of merit, ZT, of the studied compounds within the temperature range of 340 K < T < 1070 K. Large power factors are achieved at low Nb sub-

stitution levels. The SSR compounds present a maximum ZT value for $CaMn_{0.98}Nb_{0.02}O_3$ with ZT_{1060K} = 0.16, while for the SC series, a ZT value twice as high is obtained for the same composition (2% Nb) with ZT_{1060K} =0.32. Thus, the electrondoped manganate phases appear as potential *n*-type legs for the development of a thermoelectric oxide module and therefore to evaluate the output power and the conversion efficiency of the thermoelectric converter.

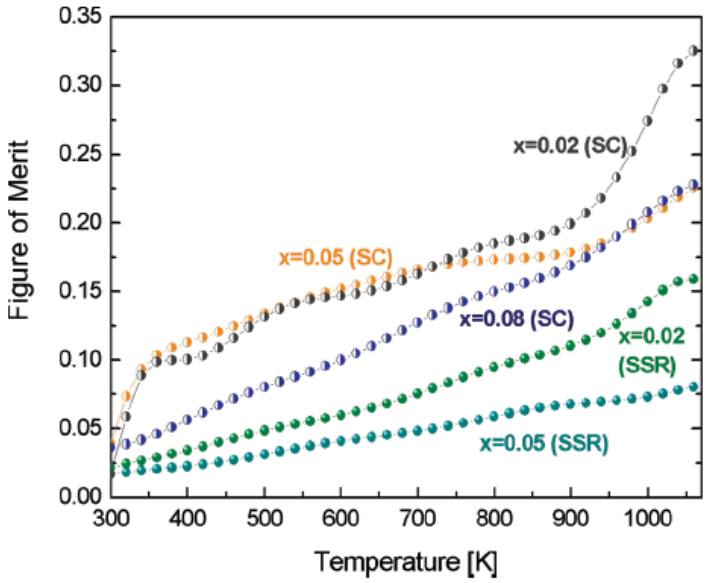

Figure 8: Temperature dependence of the figure of merit for $CaMn_{1-x}Nb_xO_{3-\delta}$ (x = 0.02, 0.05, 0.08) synthesized by both SSR (closed symbols) and SC (open symbols) methods.

Effect of the USC nanocrystallites:

The USC process was used to produce nanocrystalline manganate phases. An emphasis on their unsual low-temperature thermoelectric properties is presented. This work is further detailed in [Bocher-2007].

The ultrafine USC required lower sintering temperature (T = 1473 K) to obtain dense pellets compared to classical SSR compounds. Typical crystalline grains of 3-5 μm size are obtained by the classical SSR method. The USC particles sintered into pellets lead to nanocrystallites of 20- 50 nm diameter presenting a defined rhomboid-like shape as shown in Figure 9a). The HRTEM image displays lattice fringes corresponding to $(010)_o$ planes, in the orthorhombic framework, confirming the highly crystalline character of the manganate phases achieved from the USC synthesis.

Figure 9b) presents the magnetic data of the USC and SSR compounds. The paramagnetic Curie temperature is determined for the SSR compounds where antiferromagnetic (AFM) fluctuations dominate the paramagnetic (PM) regime for 5% Nb (Θ =-34 K) while weak ferromagnetic (FM) interactions exist for x = 0.08 (Θ = 9 K). This result reflects the introduction of weak FM interactions in the $CaMnO_3$ AFM matrix by increasing the Nb substitution. The ferromagnetism fluctuations can be explained by the double exchange (DE) phenomena [Zener-1951] between Mn^{3+}/Mn^{4+} enhanced by the Nb substitution. However, the Nb^{5+} cations

present a d^0 electronic configuration which limits the DE phenomena and prevents a long FM range ordering in the Mn sublattice [Raveau-2000]. The magnetization curves of the USC and SSR compounds show a different behavior. All the USC samples exhibit predominant AFM interactions ($\Theta < 0$) with low magnetic moment indicating a pronounced suppression of the FM fluctuations in the PM regime. The field dependence magnetization recorded for the USC and SSR $CaMn_{0.95}Nb_{0.05}O_3$ compounds at 5 K display different open hysteresis loops. The M(H) curve for the USC sample confirms the suppression of the weak FM fluctuations with low magnetic moments.

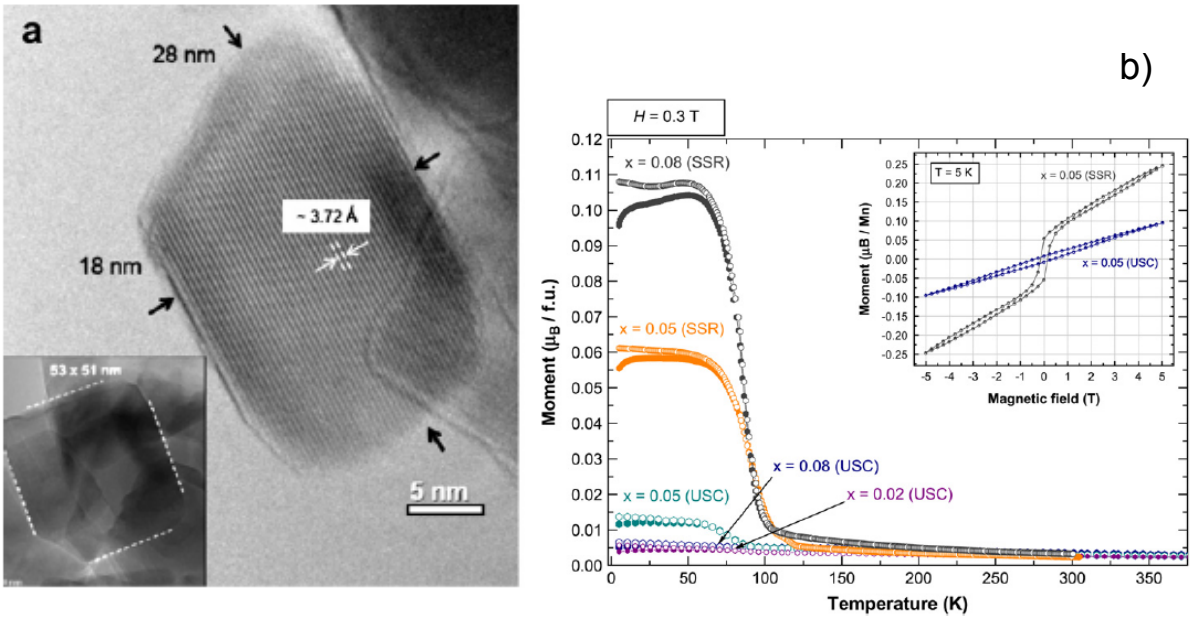

Figure 9: a) HRTEM image of $CaMn_{0.98}Nb0.02O_3$ (the inset presents a low resolution TEM image of others crystallites), b) The zero field cooled (zfc) and field cooled (fc) magnetization temperature dpendence in H = 0.3 T for $CaMn_{1-x}Nb_xO_3$. The inset presents the magnetic hysteresis loops at 5 K for $CaMn_{0.95}Nb_{0.05}O_3$ synthesised by USC and SSR methods.

Furthermore at low temperature (T < 100 K) the USC series present higher resistivity values compared to the SSR phases (for x = 0.08 at 30 K: ρ_{USC} = 598.2 Ω cm and ρ_{USC} = 18.5 Ω cm) suggesting a less ferromagnetic Mn^{3+}-O-Mn^{4+} network for the USC compounds. The USC nanocrystallites limit the DE phenomena therefore the FM interactions are strongly suppressed. Besides, the low-temperature S(T) curves, i.e., for temperature below the ordering temperature (TM), exhibit different shapes between USC and SSR phases emphasizing the different ferromagnetic strength between both series. In the case of USC compounds, the strong suppression of FM interactions induces higher ρ values and a large increase of |S|. This sudden increase of the absolute thermopower values below TM results from the limitation of the DE phenomena and the pronounced suppression of FM interactions in the USC compounds.

The USC nanocrystallite manganate phases display a pronounced FM suppression coupled to an abrupt increase of the absolute thermopower value below the magnetic ordering tem-

perature. Different hypothesis can be assumed considering either different compositions on grain boundaries or a weakening of the DE ferromagnetism phenomena due to the small size of the USC crystallites.

High temperature transition:

The higher temperature range (T >1100 K) of both A- and B-site substituted CaMnO3 has not been explored so far concerning their TE properties. The present work reports on the study of the $CaMn_{1-x}Nb_xO_3$ phases (with x = 0.02, 0.05, 0.08 and 0.10) with emphasis the temperature range of 600 K < T < 1250 K.

Figures 10 a) and b) present the high-temperature XRPD patterns of $CaMn_{0.98}Nb_{0.02}O_3$ at from 298 K to 1173 K, respectively. The reflections observed at T < 1173 K can be indexed in the orthorhombic unit cell (S.G., Pnma), while the XRPD data recorded at 1173 K can be refined using the cubic structural model (S.G., Pm-3m). The $CaMn_{0.98}Nb_{0.02}O_3$ phase undergoes a phase transition from orthorhombic to cubic structure at 1073 K < Tc < 1173 K in air.

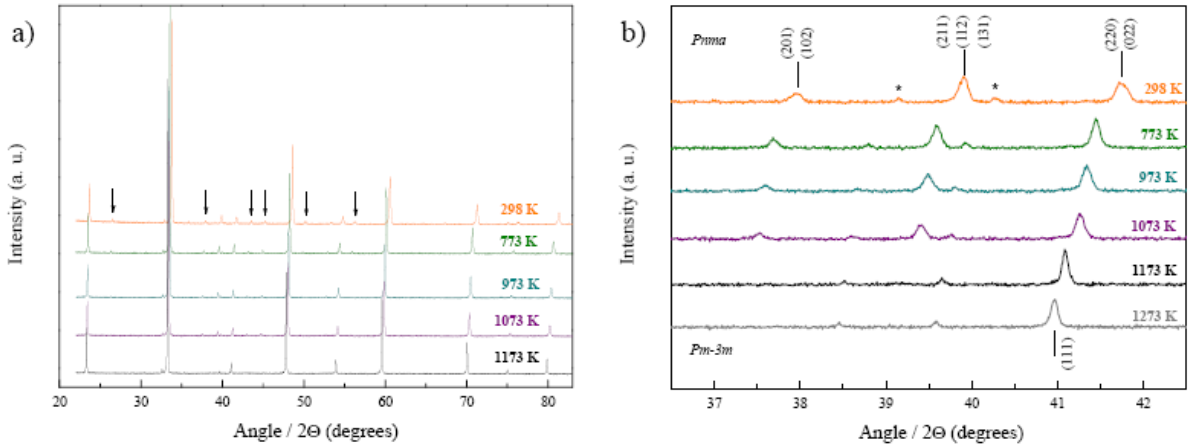

Figure 10: a) and b) In situ high-temperature XRPD patterns of $CaMn_{0:98}Nb_{0:02}O_3$ undergoes phase from 298 K to 1173 K under air atmosphere. The arrows in Figure a) indicates the reflections disappearing during the phase transition. The 36-43° 2θ range is enlarged in Figure b) emphasizing the evolution of three main reflections upon heating.

The XRPD investigations yield a general overview of the crystal structure and its evolutio with increasing temperature. In addition, TEM studies can give a better insight of the local microstructure of the studied materials. As previously reported, nano-scale twinned domains present in polycrystalline manganate phases can influence dramatically their related thermal properties, and further their TE activities [Aguirre-2008a; Bocher-2008b]. Various microstructural features such as twinned domains are frequently generated upon phase transitions that involve a change in space group symmetry. The low-temperature phases have often lower symmetry than the high-temperature ones. If the low symmetry phase belongs to a subgroup of the high symmetry one, a symmetry- breaking transition induces domain microstructure [Nord-1994].

Structural transitions in perovskite-type phases can induce oxygen deficiencies upon heating [Dabrowski-2003] or changes in thermal and transport properties while the thermal stability remains constant [Aguirre-2008b].The thermal stability of high-temperature TE oxides are of fundamental interest regarding their temperature range of applications. Thermal cycles were performed on the potential TE manganate phases [Bocher-2008b], and the influence on their TE properties was evaluated.

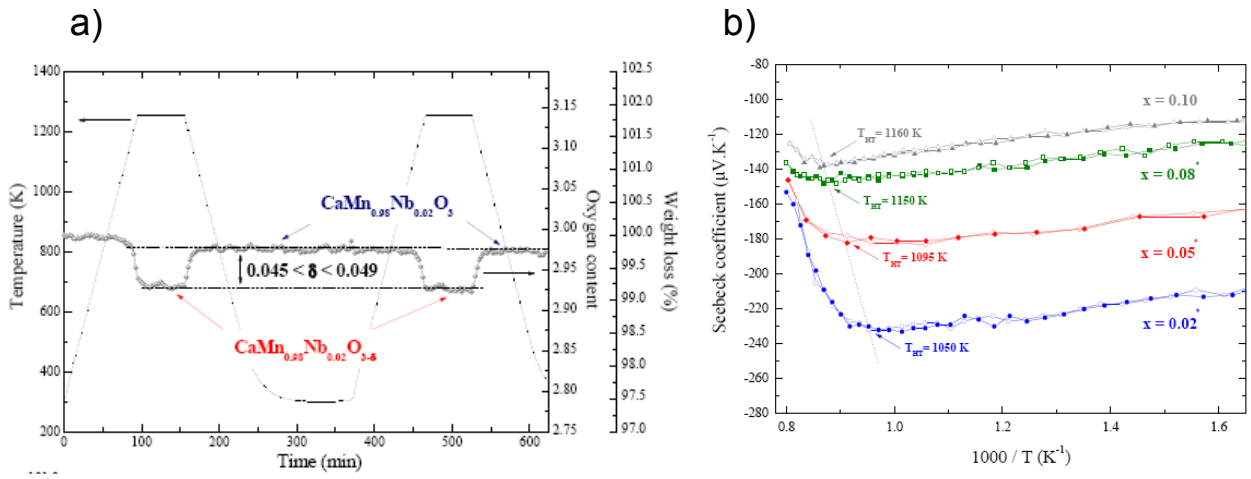

Figure 11: a) In situ thermogravimetric analysis of $CaMn_{0.98}Nb_{0.02}O_3$ phase upon heating and cooling cycles under air atmosphere (two successive thermal cycles including an one-hour isothermal step at T = 1253 K are presented) and b) Inverse temperature dependence of Seebeck coefficient for CaMn1-xNbxO3 (for x = 0.02, 0.05, 0.08 and 0.10) while heating (closed symbols) and cooling (open symbols) under air atmosphere.

Successive thermal cycles, under ambient air atmosphere, reveal a weight loss upon heating and a gain of weight upon cooling recovering the starting sample weight, as shown in Figure 11 a). Subsequent and reproducible thermal reduction and re-oxidation processes occur in the temperature range of 1080 K < T < 1100 K. From thermogravimetric data, the oxygen deficiency δ is determined equal to $0.045 < \delta < 0.049$ up to 1253 K. No further oxygen release is observed while sustaining the compound at T > Tc for an one-hour isothermal step. The structural transition and the thermal reduction are interrelated phenomena yielding to the detwinning of the orthorhombic crystal structure and to the oxygen vacancy formation, respectively. The detwinning causes structural reconstructions where domain boundaries disappear. Thus, small amount of oxygen might be released at the twinned domain boundaries to accommodate the cubic structure. Inversely, oxygen might be required at the domain boundaries during the twinning formation while cooling.

Figure 8 presents the inverse temperature dependence of the Seebeck coefficient for the $CaMn_{1-x}Nb_xO_3$ series (for x = 0.02, 0.05, 0.08 and 0.10). Equal thermopower values are obtained upon heating and cooling processes under ambient air atmosphere. This finding indicates that any gradual deterioration of the compounds and their related TE properties occur after several thermal cycles up to 1273 K.

5. Conclusions

The research of functional thermoelectric oxide materials remains a great challenge in the framework of the renewable energy technologies. The present study has evidenced new promising n-type thermoelectric manganate phases able to operate in air at high temperatures. Introducing nanosized twinned domains in the SC phases can act as scattering centers effective for the phonons but ineffective for the charge carriers. A complete homemade thermoelectric oxide module (TOM) composed of *p*-type cobaltate [Robert-2007b] and *n*-type manganate [Bocher-2008b] phases has been already fabricated considering different technological criteria such as the thermoelement lengths, the electrical contact resistances, the thermal dilatation between the interface materials [Tomes-2008].

Complementary studies on the thermal stability under long-term process are essential to investigate further prospective TE properties of electron-doped manganate phases.

Here it was shown that an enhancement of the ZT values by at least an order of magnitude is possible in these novel unconventional materials. Nevertheless, still a lot of effort has to be invested to enhance the thermoelectric activity and stability of the material to develop improved thermoelectric converters for sustainable energy technologies.

References

[Aguirre-2008a] M. H. Aguirre, S. Canulescu, R. Robert, N. Homazava, D. Logvinovich, L. Bocher, Th. Lippert, M. Döobeli, and A. Weidenkaff, J. Appl. Phys., 2008, 103, 013703.

[Aguirre-2008b] M. H. Aguirre, D. Logvinovich, L. Bocher, R. Robert, S. G. Ebbinghaus, and A. Weidenkaff, Acta Mater., 2008.

[Bleloch-2004] A. Bleloch and A. Lupini, Mater. Today, 2004, 7, 42-48.

[Bocher-2006] L. Bocher, R. Robert, M. H. Aguirre, L. Schlapbach, and A. Weidenkaff, Proc. 4th European Conference on Thermoelectrics, 2006.

[Bocher-2007] L. Bocher, M. H. Aguirre, R. Robert, M. Trottmann, D. Logvinovich, P. Hug, and A. Weidenkaff, Thermochim. Acta, 2007, 457, 11-19.

[Bocher-2008a] L. Bocher, R. Robert, M. H. Aguirre, S. Malo, S. H_ebert, A. Maignan, and A. Weidenka_, Solid State Sciences, 2008, 10, 496-501.

[Bocher-2008b] L. Bocher, M. H. Aguirre, D. Logvinovich, A. Shkabko, R. Robert, M. Trottmann, and A. Weidenkaff, Inorg. Chem., 2008, 47, 8077-8085.

[Dabrowski-2003] B. Dabrwoski, O. Chmaissem, J. Mais, S. Kolesnik, J. D. Jorgensen, and S. Short, J. Solid State Chem., 2003, 170, 154-164.

[Flahaut-2006] D. Flahaut, T. Mihara, R. Funahashi, N. Nabeshima, K. Lee, H. Ohta, and K. Koumoto, J. Appl. Phys., 2006, 100, 084911, 1-4.

[Galasso-1969] F. S. Galasso, Structure, Properties and Preparation of Perovskite-type Compounds; Pergamon Press Ltd.: Oxford, 1969.

[Hejtmanek-1999] J. Hejtm_anek, Z. Jir_ak, M. Marysko, C. Martin, A. Maignan, M. Hervieu, and B. Raveau, Phys. Rev. B, 1999, 60, 14057-14065.

[Hicks-1993] L. D. Hicks, and M. S.Dresselhaus, Phys. Rev. B, 1993, 47, 12727-12731.

[Maignan-1998] A. Maignan, C. Martin, F. Damay, and B. Raveau, Phys. Rev. B 1998, 58, 2758-2763.

[Nord-1994] G. L. Nord Jr., Phase Transitions 1994, 48, 107-134.

[Ohta-2006] S. Ohta, H. Ohta, and K. Koumoto, J. Ceram. Soc. Jpn. 2006, 114, 102-105.

[Raveau-2000] B. Raveau, Y. M. Zhao, C. Martin, M. Hervieu, A. Maignan, J. Solid State Chem. 2000, 149, 203-207.

[Robert-2007a] R. Robert, L. Bocher, B. Sipos, M. Döbeli, A. Weidenkaff, Prog. Solid State Chem. 2007, 35, 447-455.

[Robert-2007b] R. Robert, M. H. Aguirre, P. Hug, A. Reller, A. Weidenkaff, Acta Mater. 2007, 55, 4965-4972.

[Thao-2003] P. X. Thao, T. Tsuji, M. Hashida, and Y. Yamamura, J. Ceram. Soc. Jap. 2003, 111, 544-547.

[Terasaki-1997] I. Terasaki, Y. Sasago, and K. Uchinokura, Phys. Rev. B 1997, 56, R12685-R12687.

[Tomes-submitted] P. Tome, R. Robert, M. Trottmann, L. Bocher, M. H. Aguirre, J. Hejtmanek and A. Weidenkaff, Submitted 2008.

[Wang-2006] W. L. Wang, and H. Y. Lu, J. Am. Ceram. Soc. 2006, 89, 281-291.

[Weidenkaff-2004] A. Weidenkaff, Adv. Eng. Mater. 2004, 9, 709-714.

[Zener-1951] C. Zener, Phys. Rev. 1951, 82, 403-405.